Deployment Dynamics of Foldable Thin Shell Space Structures

Antonio Pedivellano * and Sergio Pellegrino.†
California Institute of Technology, Pasadena, CA, 91125.

This paper investigates the deployment behavior of lightweight flexible space structures consisting of thin shell components. An extensive and detailed study of a symmetrically folded structure that dynamically deploys by releasing its stored elastic energy is presented. The challenges involved with ground testing of this structure are discussed, and a suspension system that allows propagation of the elastic folds is proposed. The dynamics of two 1 m-scale structural prototypes was measured using high-speed Digital Image Correlation. It is shown that, for the tests considered, the elastic folds remain stationary and behave as elastic hinges, resulting in a symmetric and repeatable deployment. Deployment experiments in air and vacuum showed that air mass significantly affects the dynamics of the structure, slowing its deployment by 70 %. However, this effect becomes negligible if the deployable structure is not covered by a film. A finite element model of the deployment is presented. The effects of air are approximated by an added mass to the structure, calculated through simple geometric arguments. This model shows good agreement with experimental results without increasing the associated computational time.

I. Introduction

Solar arrays account for a significant portion of deployable structures for space applications. They are often based on a strip architecture, consisting of several rigid panels connected by hinges, forming large rectangular planar surfaces when deployed. Packaging generally involves folding the panels about their hinges, and deployment can be driven either by external mechanisms [1][2] or by releasing the strain energy stored in elastic hinges [3][4][5]. Figure 1 shows two alternative folding concepts. Z-folding consists of alternating mountain and valley folds in an accordion-like fashion, and has been used in most foldable spacecraft structures flown so far, like the 34 m $\times$ 12 m solar arrays of the International Space Station [6]. Tri-folding consists of folding the panels in the same direction; typically, there is a central panel on top of which two side panels are folded, hence the name. This folding method has been used in CubeSats, e.g. MarCO [7] and OMERA [5], where the solar panels are initially folded parallel to the faces of the spacecraft, or in combination with z-folding, such as in the Folded Integrated Thin Film Stiffener (FITS) array, demonstrated by AFRL on the TacSat-2 mission [8].

Recent advances in flexible solar cells, like perovskite cells [12], and in flexible electronics [13] offer the opportunity to develop new structural paradigms that reduce mechanical complexity, mass, packaged volume and, ultimately, cost. One promising path is the use of thin shell structures, which are already widely used for deployable booms [14][15]. The geometry of thin-walled shell cross sections provides high bending stiffness when deployed, while also allowing elastic folding and packaging in small volumes. Using thin shell components to support flexible functional elements, a novel class of deployable strip architectures can be developed.

The recent Roll-Out Solar Array (ROSA) flight demonstration [16], flown in 2018 by AFRL, consisted of a flexible blanket containing solar cells and supported by two thin-shell composite slit tubes. The 5.4 m $\times$ 1.7 m array was initially coiled in a cylindrical configuration, and then self-deployed by the controlled release of elastic strain energy in the deployable booms. This successful experiment demonstrated the potential for a new generation of deployable structures with superior packaging capabilities and area-to-mass ratios.

So far, much focus has been placed on packaging through coiling, which is a mainstream solution for deployable boom applications [17][18]. In general, coiled shell structures require a deployment mechanism to support them and to constrain them in order to prevent accidental self-deployment. The smallest size of the mechanism depends on the maximum strain the shell structure can tolerate, and scales well with the size of the structure. Hence, because the packaging efficiency of coilable architectures increases with the size of the structure, this approach is less attractive for

*Graduate Student, Graduate Aerospace Laboratories, 1200 E. California Blvd, MC 105-50. AIAA Student Member. E-mail: apedivel@caltech.edu

†Joyce and Kent Kresa Professor of Aerospace and Civil Engineering, Graduate Aerospace Laboratories, 1200 E California Blvd. MC 105-50. AIAA Fellow. E-mail: sergiop@caltech.edu

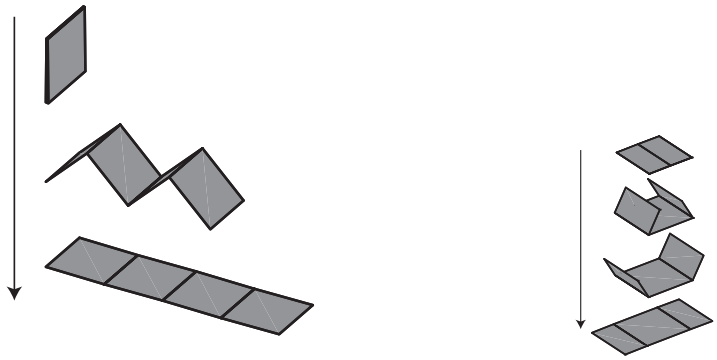

(a) Z-folding (accordion-type folding) of a solar array [9] [10]

(b) "Tri-fold" packaging concept [11]

Fig. 1 Packaging concepts for foldable strip architectures with rigid panels.

small scale applications, e.g. CubeSats [19], which are often constrained by volume and cost. In these cases, packaging schemes based on discrete folds, as shown in Fig. 1 might offer a better alternative, as they require simpler and smaller deployment mechanisms, such as burn wires [20] or pin pullers [21]. Moreover, concepts of deployable structures consisting of combinations of many flexible strip units have been proposed [22], for use in space solar power applications. In this case, the geometry of the structure requires a combination of folding and coiling to achieve the fully stowed configuration. Therefore, the present work focuses on the mechanical behavior of folded flexible strip structures.

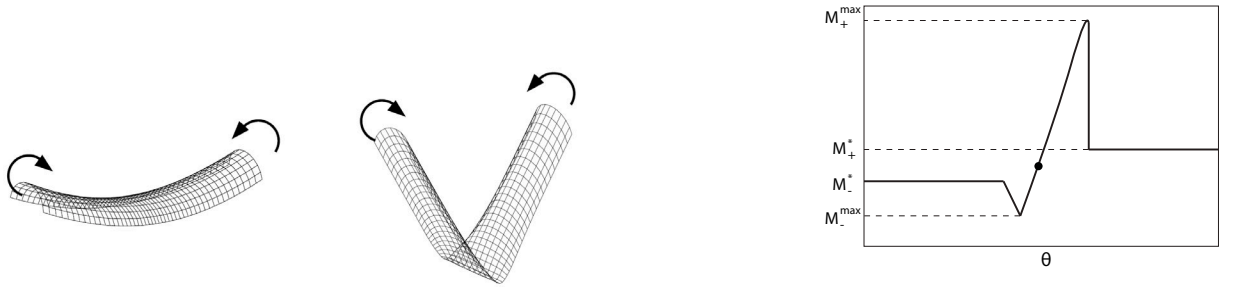

(a) Localized folds in a tape spring (image adapted from [23])

(b) Schematic moment-rotation relationship for a tape spring

Fig. 2 Non-linear mechanical response of a tape spring under bending. After the initial linear behavior, a snap-through instability leads to the formation of localized folds.

The problem of folding and deploying a thin shell structure has been extensively studied in the past for tape springs, i.e. cylindrical shells with a circular arc cross section. Under applied bending moments, these structures exhibit a non-linear mechanical response and undergo snap-through instabilities, resulting in localized deformations. Figure 2(a) shows two geometric configurations of a tape spring. For small applied rotations, the tape spring deforms uniformly. At the buckling limit, the cross-section of the tape spring flattens in a small region, creating an elastic fold. Figure 2(b) shows a notional moment-rotation relationship for a tape spring: after the initially linear response, the bending moment drops and becomes mostly independent of the applied rotation. The first documented study of the geometry of elastic folds dates back to the 1920s [24], although models to predict the moment-rotation relationship were published only in the 1950s by Wuest [25], and later expanded by Rimrott [26] and Mansfield [27] in the 1970s. In 1999, Seffen et al. [23] investigated the dynamics of initially folded tape springs during strain energy-driven deployment. Their study showed that elastic folds propagate along the axis of the shell, resulting in a complex but predictable deployment behavior.

More recently, the dynamic deployment of foldable tubular shells with longitudinal cutouts to create elastic hinges at set locations has been explored [28]. This structural concept has been successfully implemented in the 20 m-long antennas on board the MARSIS spacecraft [29].

The existing literature has focused on independent thin shell components, either with a single elastic fold or with multiple folds whose propagation is prevented by the geometry of the shell (as in the case of foldable tubes). Further developments of foldable strip architectures will involve the deployment of shell structures with multiple propagating folds, or the interaction between two or more shells.

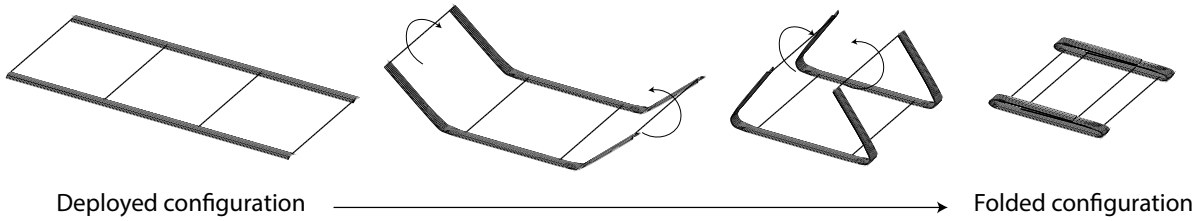

Fig. 3 Concept of foldable strip with tape spring longerons.

The latter is the focus of the present work. In particular, this paper considers a flexible strip consisting of two thin shell longerons, connected at discrete points by transverse rods. This ladder-like structure, previously studied by Royer and Pellegrino [30], is folded at two locations as shown in Fig. 3, similarly to the tri-fold scheme in Fig. 1. The objective of this paper is to develop an experimental and computational framework to characterize and predict the deployment dynamics of flexible strip structures. Methods and techniques previously developed for thin shells and rigid deployable structures will be combined to address some unique challenges associated to the behavior of flexible strips.

To enable experimental investigations of dynamic deployment that can be used to validate numerical simulations, a simple suspension system characterized by low inertia and friction, and robust against variations of the strip geometry due to propagation of the elastic folds was developed. 3D Digital Image Correlation (DIC) was used to characterize the deployment experiments, and an algorithm to identify the elastic folds and track their propagation was developed. Also, the influence of air on the dynamic deployment of the strips was investigated by performing deployment experiments both in air and in vacuum. The effects of having a flexible film on the tested strip, representing functional elements in an actual structure, was also studied. Regarding the computational approach, a high-fidelity finite element model of the strip deployment was developed, which includes the effects of air in the dynamics of the structure.

The paper is organized as follows. Section II describes the geometry of the strip and the suspension system designed for the deployment experiment. In Section III, the implementation and characterization of the experimental setup are discussed. In Section IV, the experimental results are presented; the effect of a thin film on the strip, as well as the influence of air during ground deployment, are addressed. Section V describes the finite element model of the strip, discussing the simulation technique and the simulation parameters. Section VI presents the results from the simulations and compares them with experiments. Finally, Section VII discusses the results and concludes the paper.

II. Problem Description

A. Strip Design

The flexible strip architecture developed for this study is shown in Fig. 4. Two thin shell longitudinal elements, herein called "longerons", provide bending stiffness to the deployed strip, and can be folded by forming elastic folds for packaging. They have an open cross section consisting of two circular arc flanges, connected by a flat web region. This cross section design, first introduced in TRAC (Triangular Rollable And Collapsible) booms [31] is symmetric about the bending axis (y-axis in Fig. 4), so that the moment-rotation relationship is independent of the folding direction. The longerons are connected by transverse rods, called "battens", which have a rectangular cross section. The battens are responsible for the bending stiffness of the strip in the y-direction, as well as for providing coupling between the longerons. The resulting ladder-like structure constitutes the backbone of the strip and supports a thin film that in an actual application would support functional elements, such as solar cells or RF antennas. The strip is supported at its ends by cords, connected to two rigid connectors mounted in the middle of the outermost battens. The next sub-section provides more details about the suspension system.

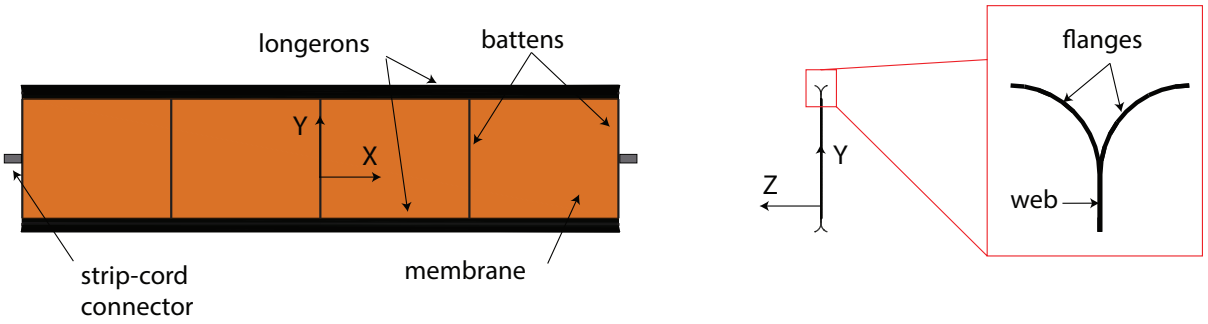

Fig. 4 Strip geometry: top view (left); side view and detail of the TRAC longeron geometry (right).

B. Suspension System Concept

Using ground testing to predict the performance of lightweight deployable structures in space is a challenging task. Due to the relatively low stiffness of such structures, gravity can have a significant impact, and minimizing its effects has been the focus of extensive research. Although drop towers [32] [33] and parabolic flights [34] [35] are sometimes used to achieve micro-gravity, in most cases deployable structures are supported during ground testing by suspension systems. Generally, these systems consist of vertical cords attached to discrete points of the structure, applying a total force equal to its weight. In the simplest case, the cords can be attached to a fixed point [9][36] and soft springs can be used to allow extension of the cords with minimal variation of their tension, Fig. 5(a). To avoid the resulting in-plane forces, nested fly beams have been proposed, creating a "marionette"-like suspension [37]. However, this approach is better suited for small displacement experiments, such as vibration testing. For large-displacement deployment experiments, the cords are generally attached to sliders following the structure, in order to remain vertical at all times, Fig. 5(b). The main drawback of this solution is that the additional inertia and the friction in the sliders can significantly affect the deployment [38]. These effects can be avoided using active gravity compensation systems [39], which allow for zero-stiffness rigid body motion, zero-friction and minimal added mass. However, such systems involve significant mechanical complexity and are generally adopted for heavier structures with simpler kinematics.

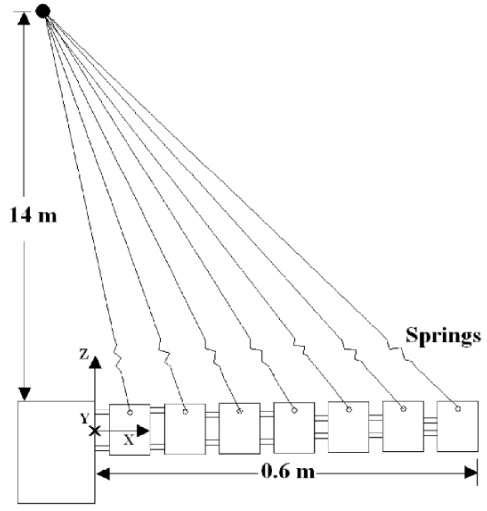

(a) Single point suspension system for z-folded rigid solar array [9]

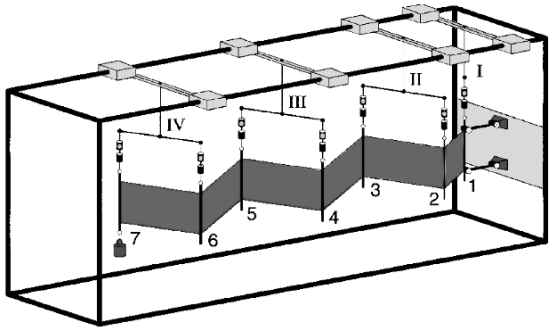

(b) Gravity offloading with sliding flybeams during deployment of a z-folded rigid solar array [38]

Fig. 5 Examples of passive gravity compensation schemes for ground deployment of folded rigid solar arrays.

For the flexible strip studied in this paper, a passive suspension system was chosen due to its simplicity and the potential for accurately modeling its interaction with the structure during deployment. However, the presence of elastic

folds made it challenging to implement any of the concepts shown in Fig. 5, which are deployed in a plane normal to the direction of gravity. Equilibrium of the moments requires each cord to be attached above the center of gravity of the portion of the structure being supported, at any time. For example, in the event of propagation of the elastic folds, the center of mass of the structure would shift, resulting in an unbalanced configuration that would cause the rotation of the plane of deployment. Hence, rather than trying to minimize the effects of gravity on the structure, which would have required a highly complex gravity offloading system in the case of structures with propagating elastic folds, it was decided to devise a simpler suspension system, whose main purpose is to allow a deployment under gravity to be successfully completed.

In this scheme, by orienting the structure with the gravity vector normal to the plane of the deployed strip (z-direction in Fig. 4), unbalanced gravity-induced moments would not cause rotation of the deployment plane. Also, supporting the strip only from the ends minimizes any interactions between external loads and elastic folds.

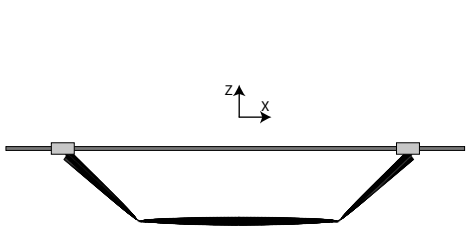

(a) Sliding ends

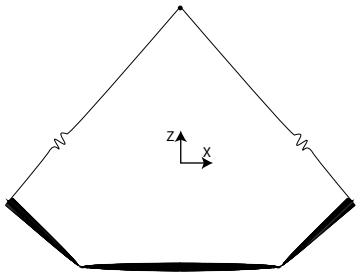

(b) Single point cord suspension system with soft springs

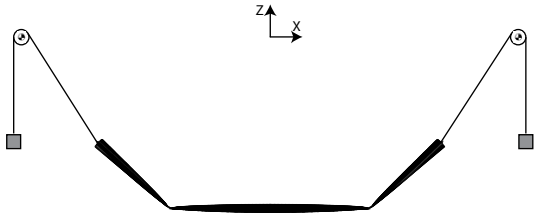

(c) Cord suspension system with counterweights for upward deployment

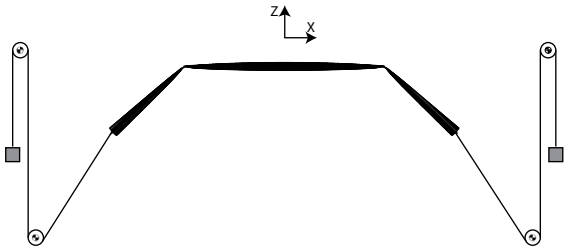

(d) Cord suspension system with counterweights for downward deployment

Fig. 6 Side views of suspension system concepts for ground deployment of foldable flexible strips.

Several implementations of the support system were considered, see Fig. 6. Using sliders, as shown in Fig. 6(a) and similarly to the concept in Fig. 5(b), would simplify the trajectory of the ends of the strip; however, their added mass could be significant, and their friction challenging to characterize. Figure 6(b) shows two end cords attached to a single point, similarly to the concept in Fig. 5(a). Although this solution would add very small mass to the strip, the resulting in-plane forces would counteract the elastic moments in the elastic folds, likely preventing deployment of the structure. An alternative solution is to connect each cord to a pulley, and to use masses to apply tension to the cords and compensate for the weight of the strip. This concept can be used to deploy the strip in 2 different orientations, i.e. against gravity, Fig. 6(c), or assisted by gravity, Fig. 6(d). However, the latter case requires 2 sets of pulleys, thus increasing added inertia and friction. Therefore, the concept in Fig. 6(c) was chosen. Its implementation will be discussed in the next section.

C. Design of Suspension System

The schematics of the suspension system and the key parameters required to fully define a deployment experiment are shown in Fig. 7. As it will be discussed in greater detail in the next sub-section, the present study has focused on 1 m-scale strips, with a suspended mass on each side ranging between 20 g and 50 g. The distance between the pulleys

was chosen to be $L_f = 1300$ mm, to provide enough clearance for the structure during deployment.

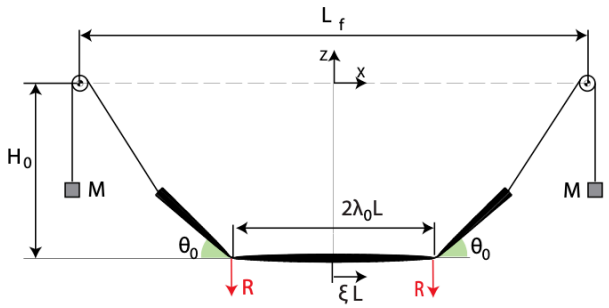

Fig. 7 Geometry and design parameters of the suspension system developed for the deployment experiments.

When the strip is in the folded configuration, additional forces are required, indicated by R in Fig. 7. These additional constraints are provided by a release mechanism, and are instantaneously released to initiate deployment. The folded configuration of the strip can be described in terms of the position and angle of its elastic folds. To reduce the size of the parameter space for the problem and simplify the numerical analyses, the present study has considered initially symmetric configurations of the structure. In this case, the initial geometry is defined by the the distance between the folds $2\lambda_0 L$, with $\lambda_0 \in [0, 1]$ (where $\lambda_0 = 0$ corresponds to having a single fold at the center of the strip), and the angle of the folds θ_0. For this experiment, λ_0 is set by the position of the release system, whereas θ_0 is not controlled directly, but it depends on the distance H_0 between the center of the strip and the pulleys, as shown in Fig. 7, and the mass M of the counterweights attached to the cords.

The choice of admissible ranges for these parameters was based on theoretical predictions. For the strips considered herein, initial heights $H_0 \in [250$ mm, 750 mm] and masses $M \in [20$ g, 100 g] allow to span a range of fold angles between 10° and 60°. After a preliminary experimental campaign to explore the parameter space defined by λ_0, H_0 and M in the range of values defined above, it was observed that the qualitative behavior of the strip during deployment does not vary significantly for most combinations of those parameters. Hence, this paper focuses on one specific set of parameters ($H_0 = 400$ mm, $M = 50$ g, $\lambda_0 = 0.45$), corresponding to an intermediate point of the parameter space, but representative of the behavior of a wider range of initial conditions.

III. Experimental Setup

A. Strip Prototypes

Two strip prototypes were manufactured for this study, based on the architecture presented in Fig. 4. Both prototypes, see Fig. 8, have the same nominal length $2L = 1125$ mm and consist of 2 TRAC longerons, placed 200 mm apart and connected by 5 equally spaced battens. The longerons have nominal flange radius 12.4 mm, flange opening angle 90° and web width 8 mm.

The flanges were manufactured from ultra-thin composite prepregs. The stacking sequence was $[\pm 45_{GFPW}/O_{CF}/\pm 45_{CFPW}]$, where GFPW represents a 402T glass fiber plain weave (25 gsm) provided by JPS Composite Materials, and CF denotes a unidirectional MR70 carbon fiber (30 gsm). Both laminates had been pre-impregnated with CE380 cyanide ester resin by Patz Materials and Technologies. An additional $[\pm 45_{GFPW}]$ bonding layer is interposed between the flanges in the web region. This laminate design has been previously shown to induce low stress concentration during coiling of TRAC longerons [40] and has been mechanically characterized [41].

The battens consist of pultruded carbon fiber rods, with a 3 mm × 0.6 mm rectangular cross section. They are connected to the web of the longerons by Ω-shaped sleeves, made of 2-ply glass fiber composites. The strips are supported at the ends by PTFE-coated glass fiber cords, attached to 3D-printed plastic connectors, bonded to the center of the terminal battens. The two strip prototypes nominally differ only for the presence of a 50 μm-thick Kapton film bonded to the web of the longerons on one of the prototypes. This film plays the role of a functional element surrogate, and it was intended to simulate the effect of the functional element layer on the deployment dynamics of the shells.

The geometry of the strip was measured with a FaroArm laser scanner, from which the actual radius and opening angle of the TRAC longerons were extracted. The measured geometry, as well as the measured mass properties of the strips, are reported in Table 1.

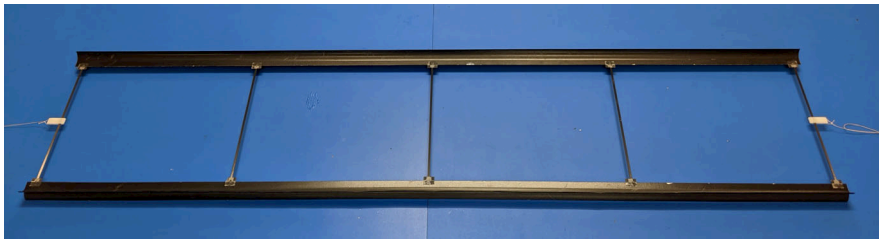

(a) Strip 1: structure without membrane

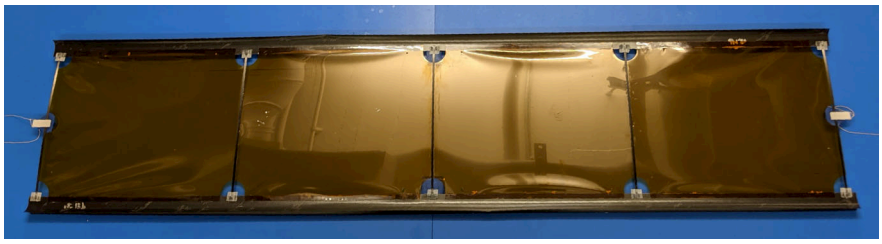

(b) Strip 2: structure with membrane

Fig. 8 Strip prototypes.

	Flange radius [mm]	Flange angle [°]	Total mass [g]
Strip without membrane	12.4 ± 0.7	91.2 ± 4.6	23
Strip with membrane	13.1 ± 1.1	80.3 ± 3.2	46

Table 1 Geometry and mass of strip prototypes.

B. Strip Characterization

The mechanical response of the strip prototypes was characterized using large-rotation bending tests [42]. The objective was to measure the bending moments at the end of the test sample as a function of the applied rotation during quasi-static unfolding of a strip with an elastic fold. This quantity is of great importance for this study, as it drives the self-deployment of the structure.

The experiments were performed on a bending machine, consisting of two sliders moving along two orthogonal directions, as shown in Fig. 9. Two regions of the strip, spaced about 400 mm apart, were connected to the sliders using acrylic clamps (grey in the figure). Note that the clamps were not symmetric with respect to the ends of the strip, to avoid having a localized fold on the central batten, which has been shown to increase the strain energy in the structure as well as the end moments. One of the sliders can freely slide and rotate about the y-axis, but does not allow rotations about the z-axis (which is the bending axis). The other slider can translate and rotate about the x-axis; rotation about the z-axis is controlled by a motor. Each slider is equipped with air bearings to reduce friction, and a force sensor to measure all force and moment components applied by the structure.

The strips were initially folded to an angle of 35°, and the elastic fold was manually placed at its center. Then, a rotation in the opposite direction was applied in small increments, until the strip had fully deployed. The results of the unfolding experiments are reported in Fig. 10. Each experiment was repeated 3 times, showing a consistent behavior.

It was observed that the fold undergoes shape and position changes during the unfolding process. Specifically, for angles greater than 15°, the fold is symmetric and the bending moment is mostly constant, slightly decreasing with the angle. At approximately θ =15°, a sudden increase in the bending moment corresponds to a change in the shape of the fold, which switches from a symmetric to an asymmetric configuration. The moment keeps increasing until it reaches a peak for $\theta \approx 3°$, after which the fold disappears and is replaced by local buckling of the longeron flange on the compression side. Both strips exhibit similar qualitative behavior, although some quantitative differences can be identified. For $\theta > 15°$, the bending moment in the strip without membrane is about 15% higher than the one with membrane, which can be explained by its larger flange angle, see Table 1. However, the strip with membrane has 30% higher peak moment. This is related to the fact that the folds on the two longerons disappear at the same time on the strip with membrane, unlike the strip without the membrane, possibly due to the additional coupling between the longerons

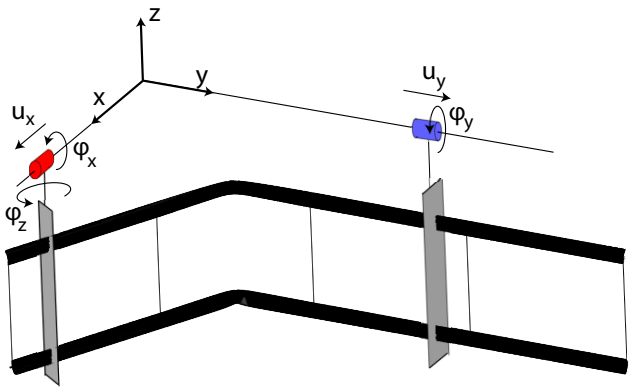

Fig. 9 Schematics of experimental setup for strip bending tests.

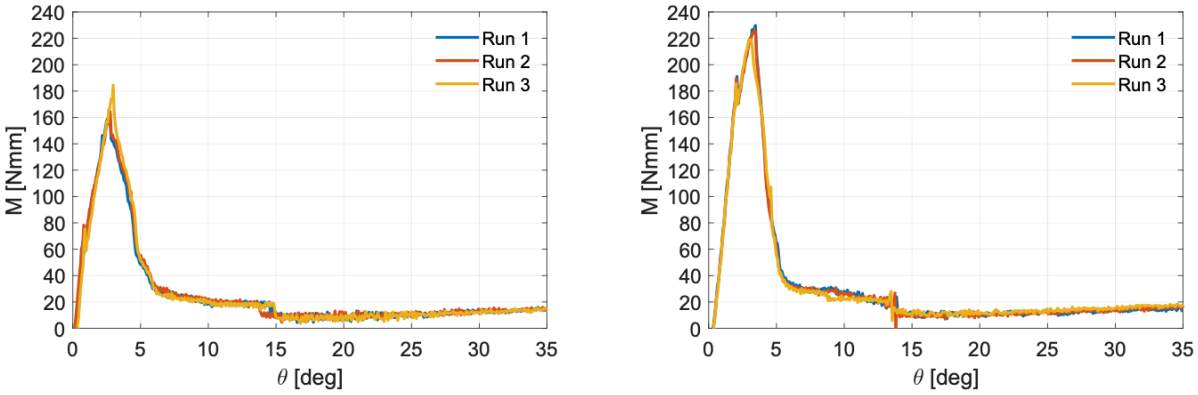

(a) Bending test of strip without membrane

(b) Bending test of strip with membrane

Fig. 10 Moment-rotation relation for the two strip prototypes.

introduced by the membrane.

C. Experimental Apparatus

The experimental apparatus consists of the suspension system, the release mechanism and the metrology system. It is shown in Fig. 11.

The suspension system includes two miniature pulleys with diameter of 12.4 mm made of nylon to reduce the inertia and mounted on ball bearings to minimize friction. The pulleys are installed on a support structure consisting of aluminum T-slotted frames. By varying the height of the pulleys from the ground, the initial fold angle of the strip can be adjusted, as previously discussed in Sec. II.C. It was shown by analysis that the inertia of the pulleys contributes to less than 1% of the total inertia of the system, and hence its effect is negligible. However, the analytical model suggested that friction in the ball bearings can significantly affect the dynamics of the suspension system. Hence, a detailed characterization of the friction of the system was performed, and will be discussed in the next sub-section.

The release mechanism is responsible for holding the strip in its folded configuration and releasing it on command to initiate deployment. The actuation is provided by two R12X12 DC pull-type linear actuators (24 V, 2.5 W) manufactured by Magnet-Schultz of America. They consist of solenoids that pull a central magnetic shaft when powered. The actuators are connected in parallel to a power supply, in order to achieve synchronized release. Preliminary tests have shown that synchronization can be achieved within 2 ms. The strip is connected to the release actuators by cords with negligible mass. Specifically, two cords run across the strip and are attached to the web of the longerons; their location along the strip defines the initial position of the elastic folds. A cord loop runs between the center of each cord and

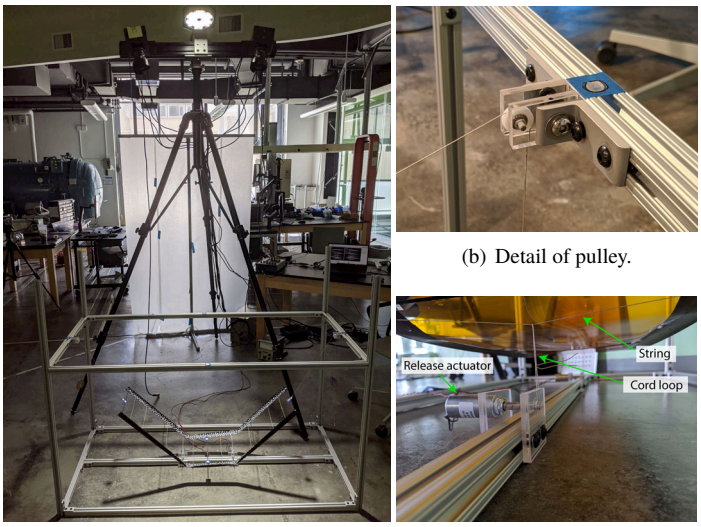

(a) Experimental setup with metrology system. (b) Detail of pulley. (c) Detail of release mechanism.

Fig. 11 Experimental apparatus for strip deployment tests.

the shaft of the corresponding release actuator, and is held taut by the counterweights of the suspension system. By retracting the shaft of the actuators, the cord loops are released, initiating the deployment.

Lastly, the metrology system consists of a high speed stereo camera system, composed of two Photron UX100 cameras set at a frame rate of 500 fps, to acquire monochrome images. The stereo system was designed to provide 1.2 m field of view with 500 mm depth of field. A 72,000 lumens REL Sure Bright module with 120 white LEDs completes the setup. A speckle pattern was applied to the top face of the TRAC longerons, with approximate speckle size of 5 mm, to perform Digital Image Correlation (DIC) on the image pairs obtained from the experiment. Also, photogrammetry was used to extract the coordinates of several targets placed on the strip and the aluminum frame, and they were used to define a coordinate system for the experiment. Both DIC and photogrammetry were performed using the VIC3D software.

The experimental setup described so far was used to perform deployment experiments of the strip prototypes both in air and in vacuum. The experiments in vacuum were performed in an altitude chamber with internal volume of 2.4 m $\times$ 2.4 m $\times$ 2.4 m. During these experiments, the pressure was maintained at 55 torr (corresponding to about 7% of standard atmospheric pressure). The temperature, which was not actively controlled, varied between 20°C and 30°C.

D. Suspension System Characterization

As mentioned in the previous sub-section, friction in the suspension system was expected to affect the deployment experiments. Therefore, a simple experiment was devised to quantify the friction torque in the pulley bearings. The experimental setup consisted of two weights with different mass M_1 and M_2 attached to the opposite ends of a cord, running on the same type of pulley that was used in Section III.C, as shown in Fig. 12(a). The weights, initially held stationary, started moving vertically as soon as they were released, with the heavier weight accelerating downwards. A target placed on this weight was tracked using the high speed camera system, which acquired images at 500 fps. Photogrammetry was performed in VIC3D to extract the coordinates of the target at each frame. By projecting the coordinates along the vertical direction, the variation of the target height as a function of time was obtained, see Fig. 12(b). A 2^{nd} order polynomial fit of the form $h(t) = c_2t^2 + c_1t + c_0$ was then used to estimate the acceleration of the weight, related to the coefficient of the quadratic term, hence

$$\ddot{h} = 2c_2 \tag{1}$$

The friction torque in the system was obtained from the following equation of motion:

$$(M_1 - M_2)gR - T_f = \left[I_p + (M_1 + M_2)R^2\right]\ddot{\alpha} \tag{2}$$

where R and I_p are the radius and the second moment of inertia of the pulley, respectively, and T_f is the friction torque on the pulley. Solving for T_f:

$$T_f = (M_1 - M_2)gR - \left[I_p + (M_1 + M_2)R^2\right]\ddot{\alpha} \tag{3}$$

The angular acceleration of the pulley is given by $\ddot{\alpha} = \ddot{h}/R$ and hence, using $\ddot{h}$ from Eq. 1, it is possible to compute the friction torque T_f.

Using this method, T_f was computed for 9 different combinations of M_1 and M_2. Each experiment was repeated 3 times, and the measured accelerations were repeatable within 1.5% of their mean value. Given the relatively low angular velocity of the pulley during the experiment, it is reasonable to neglect viscous effects in the pulley, and to assume that its friction is entirely due to the elastic rolling resistance [43], which increases linearly with the normal load on the bearing. For the case shown in Fig. 12(a), the normal force F_n is given by:

$$F_n = (M_1 + M_2)g - (M_2 - M_1)\ddot{\alpha}R \tag{4}$$

In this equation, the first term on the right hand side describes the static contribution from the weight of the two masses, whereas the second term captures the inertial effects. The equation suggests that the friction torque depends on both the sum, M_{tot}, and the difference, ΔM, of the two masses. Figure 12(c) shows a quadratic polynomial fit of the measured values of T_f as a function of M_{tot} and ΔM. The plot shows that friction increases with M_{tot}, but it becomes very small if the masses are very different (as $F_n \to 0$ when $M_2 >> M_1$) or if they are very similar (in which case the velocity of the pulley is very low).

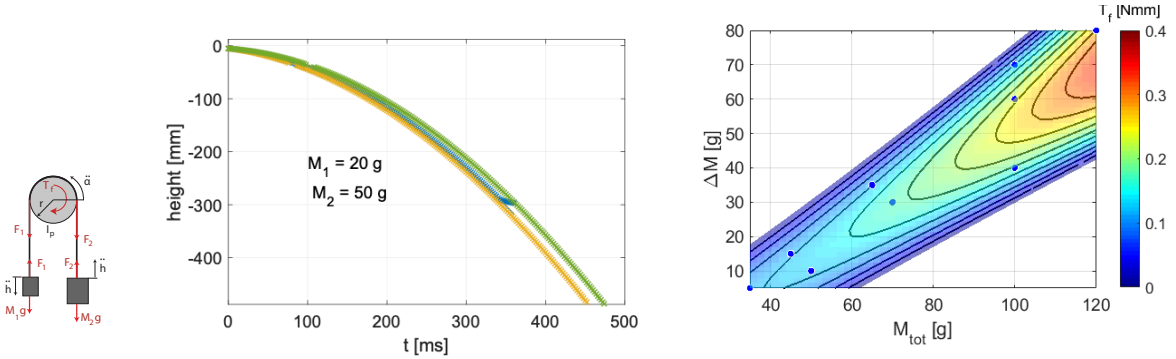

(a) Schematic of the friction characterization experiment.

(b) Example of measurements from photogrammetry for M_1 = 20 g and M_2 = 50 g. Each color corresponds to a different run of the same experiment.

(c) Measured values of friction torque T_f and fitting surface as a function of sum and difference of the two masses.

Fig. 12 Characterization of pulley friction torque.

IV. Experimental Results

Four deployment experiments were performed to test the two strip prototypes (with membrane and without membrane) both in air and vacuum. The experiments were repeated three times each, and the results were consistent. Overall, the experiments exhibited very similar qualitative behavior; Fig. 13 shows snapshots from the deployment in vacuum of the strip with membrane, starting from its initial equilibrium configuration. The strip preserved its initial symmetry throughout deployment, with the elastic folds remaining stationary and opening out monotonically. At t = 300 ms, symmetry was lost as one of the elastic folds (on the right hand side) latched into the deployed state before the other one. After both folds had fully deployed, the strip underwent a small amplitude elastic vibration, without buckling again.

The images captured by the high speed cameras were processed with DIC, which extracted a point cloud for each longeron, at each frame. An algorithm was developed in MATLAB to identify and track the elastic folds, also measuring their angle. The algorithm consists of an initialization phase, which is run on the first image taken during the experiment, and a loop, performed on all subsequent frames. The initialization consists of the following parts:

1) Define a global coordinate frame: the coordinates of 3 targets located on the aluminum frame (P_0, P_1 and P_2 in Fig. 13(a)) are extracted with photogrammetry. P_0 defines the origin, the segment P_0P_1 identifies the x-axis and the segment P_0P_2 identifies the y-axis. The axes are normalized and orthogonalized. Then, the z-axis is computed to form a right-handed coordinate system, and is positive upwards.

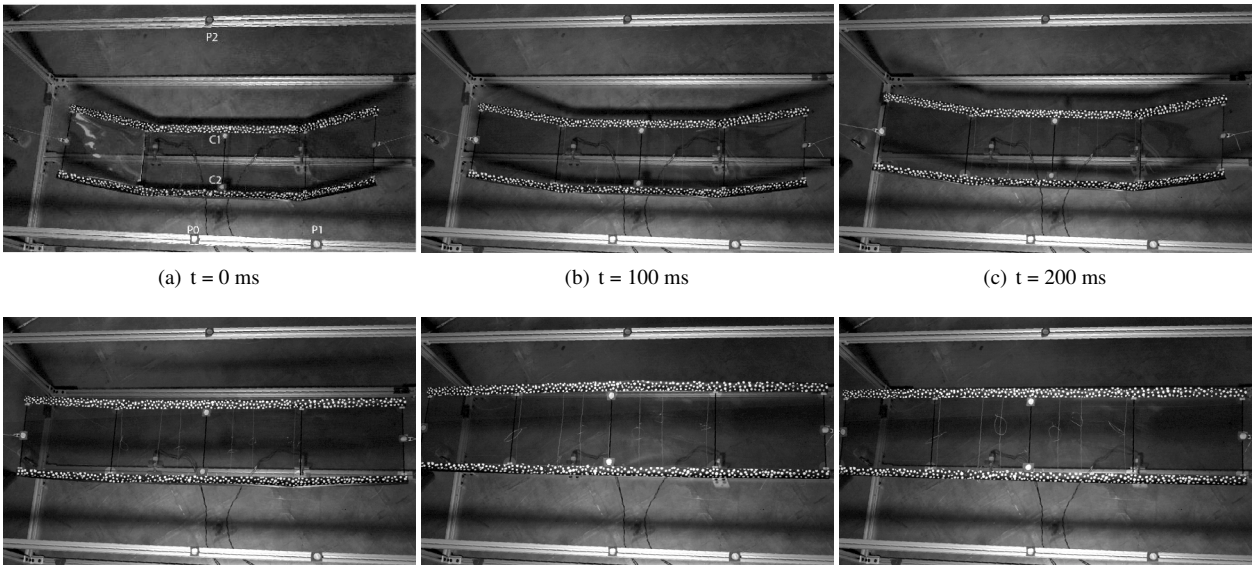

(a) t = 0 ms (b) t = 100 ms (c) t = 200 ms

(d) t = 300 ms (e) t = 400 ms (f) t = 500 ms

Fig. 13 Snapshots from deployment of a strip with membrane, in vacuum.

2) Reduce dimensionality: the point clouds are expressed in the new coordinate system, projected on the x-z plane, and sorted along the x-axis.
3) Define a curvilinear abscissa: each longeron is reduced to its mid-line by computing the median of the coordinates of a 50 points-moving window. A curvilinear abscissa is defined on the mid-line, using $s_i = s_{i-1} + \Delta s_i$, for $i = 2, ...N_p$. Here, Δs_i is the distance between 2 consecutive points on the line and N_p is the total number of points on the line. The origin of the abscissa s is defined at the center of the strip. A value of curvilinear abscissa is then assigned to each point in the cloud, by projecting it on the mid-line of the longeron and interpolating the previously computed values of s on the mid-line. Note that the curvilinear abscissa represents a body fixed frame, which identifies each point in the cloud throughout deployment.
4) Compute local tangent: the local tangent to each longeron is computed by performing Principal Component Analysis (PCA) on a 50 points-moving window from the point cloud. By performing an eigenvalue analysis on the covariance matrix of the coordinates of the points in the moving window, this algorithm returns the directions along which the points are distributed. The direction associated to the largest variance identifies, in this case, the local tangent to the longeron. The use of PCA allows to filter the noise due to some of the points being on the web and others on the flange of the longerons, resulting in a robust algorithm. Each local tangent is associated to a value of curvilinear abscissa corresponding to the median of the abscissas of the points in the moving window. By computing the dot product of the local tangents with the global x-axis, the local angle $\theta(s)$ of the longeron as a function of the curvilinear abscissa s is obtained.
5) Identify localized folds: the longitudinal curvature $\kappa(s)$ of each longeron is computed by numerical differentiation of the angle $\theta(s)$ with respect to the curvilinear abscissa, using a symmetric difference. The resulting curvature is first smoothed using a 50 point-moving average. The two highest peaks in the $\kappa(s)$ curve define the initial location of the elastic folds.

Once completed the initialization, the algorithm iterates over each frame, repeating only steps 4) and 5) of the list above. In this case, to track the localized folds, the search of the peaks in longitudinal curvature is not performed globally, but rather in a ± 20 mm region centered at the location of the folds from the previous frame. This allows to track the folds even when their longitudinal curvature becomes small (towards the end of deployment) and hard to distinguish from the noise. The outcome of the algorithm described so far is a map showing the distribution of orientation and curvature along each longeron, as a function of time. An example of these maps is reported in Fig. 14 for the deployment of the strip with membrane in vacuum. The results are very similar for the two longerons, therefore only one of them is shown. In these maps, the curvilinear abscissa on the y-axis is non-dimensionalized with respect to the length of the strip using $\xi = \frac{2s}{L}$, so that $\xi \in [-1, 1]$, with $\xi = 0$ being at the center of the strip.

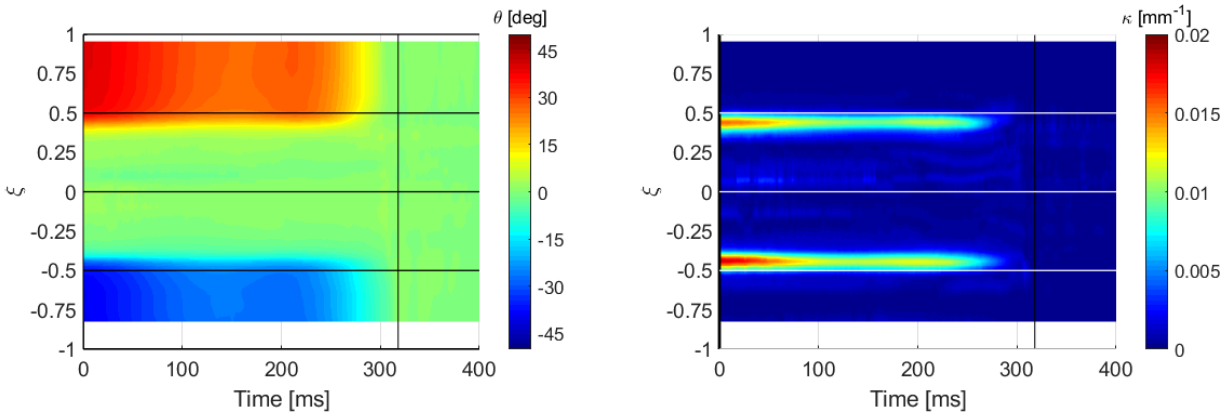

(a) Map of local orientations

(b) Map of longitudinal curvature

Fig. 14 Distribution of local orientation $\theta(\xi)$ and longitudinal curvature $\kappa(\xi)$ over time for a strip without membrane deploying in air. ξ represents a non-dimensional curvilinear abscissa, which is 0 at the center of the strip and ± 1 at the ends. Results shown for one longeron.

Fig. 14(a) shows that there are three distinct regions with uniform orientation in the longeron. Specifically, the central region is approximately horizontal, whereas the others have equal and opposite orientation, decreasing over time until the strip fully deploys. The map of curvatures shows two well-defined peaks, corresponding to the location of the elastic folds, which remain stationary during deployment. Although these maps provide a full-field characterization of the deployment process, a more compact description would allow easier comparison of the results. Therefore, in the rest of this paper, the results will be presented in terms of the angle of the folds and the height of the center of the strip, which provide insights into the dynamics of the elastic folds, as well as the rigid body translations of the structure. The angle of each fold is computed by taking the median of $\theta(s)$ between the location of the fold and the end of strip, at each time increment. The height of the center of the strip is provided by the z coordinate of two targets placed next to the center of each longeron (C_1 and C_2 in Fig. 13(a)), tracked with photogrammetry. The results for each experiment are shown in the rest of this section.

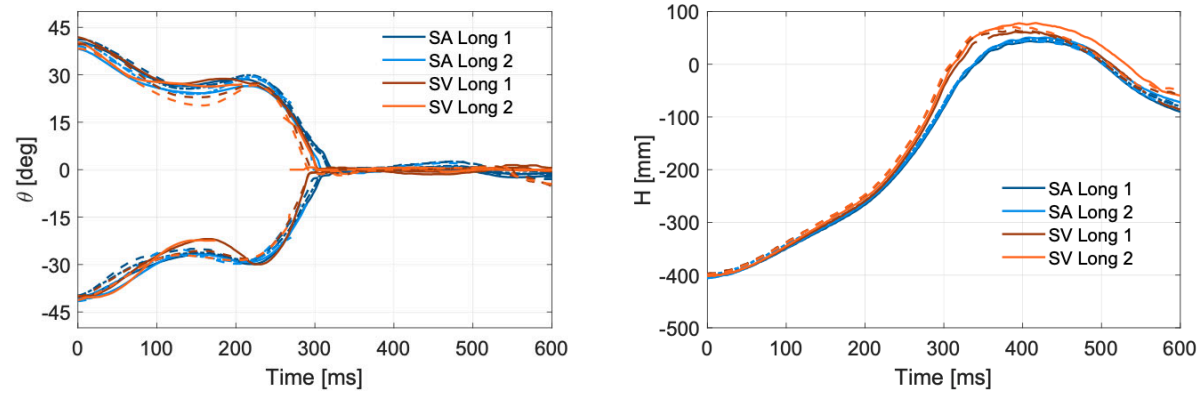

(a) Fold angle.

(b) Height of strip center.

Fig. 15 Experimental results for strip without membrane, in air (SA) and vacuum (SV). Initial conditions: M = 50 g, $\lambda_0 = \pm 0.45$, H_0 = 400 mm. Solid, dashed and dotted lines correspond to different runs of the same experiment.

Figure 15(a) shows plots of the angle of the elastic folds θ as a function of time, for the strip without membrane. Each longeron has two folds, hence the plot contains two lines starting from equal and opposite angles. Solid, dashed and dotted lines correspond to different runs of the same experiment. Also, the blue lines correspond to the tests in air,

the orange ones to the tests in vacuum. It can be observed that, overall, the tests are symmetric, with both longerons undergoing the same variation of fold angle on both folds. The fold angle starts from approximately ±42°, and then decreases until becoming zero at about $t = 300$ ms. During deployment, an oscillation of the fold angle, with a period of about 220 ms, can be observed. After reaching $\theta \approx 0°$, the localized folds disappear, and the strip vibrates undergoing uniform, small-amplitude deformations. Comparing the tests in vacuum and in air, it can be observed that there is almost no difference between them, indicating that the effects of added air mass and air drag on the unfolding process of a strip without membrane are negligible. The plot in Fig. 15(b) shows the height of the center of the strip during deployment (with the zero corresponding to the height of the pulleys). The plot shows that the height increases monotonically until the strip fully unfolds at $t = 300$ ms. After that, the structure continues to move upwards as a rigid body and it overshoots, reaching its maximum height at $t = 400$ ms. The longerons maintain the same height during deployment, indicating that there is no twisting of the strip. In this case, comparing the experiments with air and in vacuum, it can be noticed that the latter is faster than the former in the last portion of deployment (after $t = 250$ ms), and it reaches a higher peak sooner.

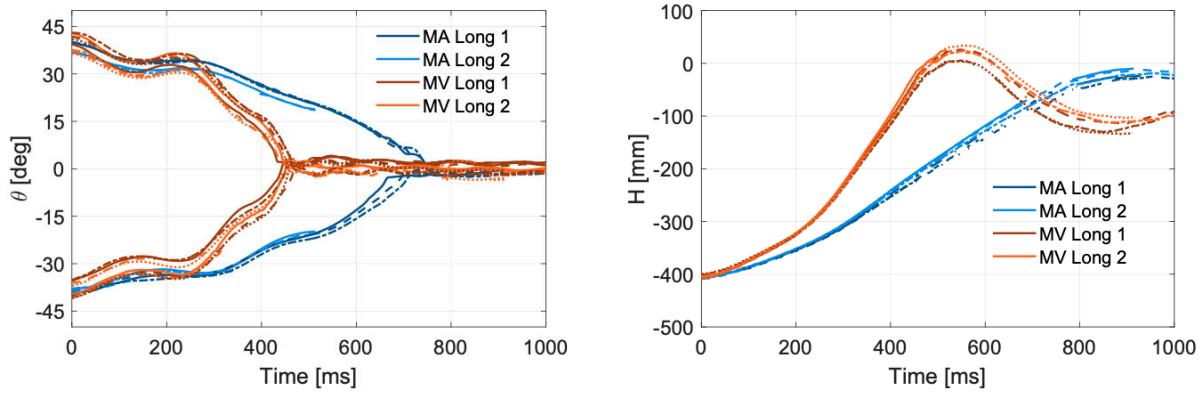

(a) Fold angle.

(b) Height of strip center.

Fig. 16 Deployment results for experiments on strip with membrane, in air (MA) and vacuum (MV). Initial conditions: $M = 50$ g, $\lambda_0 = 0.45$, $H_0 = 400$ mm. Solid, dashed and dotted lines correspond to different runs of the same experiment.

Figure 16 presents the results for the strip with membrane, both in air and in vacuum. Again, the behavior of the strip is symmetric and the three runs of the experiment were quite consistent. However, in this case, air plays a significant role, with the deployment in air being about 1.7 times slower than in vacuum (750 ms vs. 450 ms). Similarly to the strip without membrane, the fold angle oscillates during deployment. The average period of the oscillations was T = 280 ms in air, $T = 220$ ms in vacuum. Also, the amplitude of the oscillation was smaller in air than in vacuum. Figure 16(b) shows the height of the center of the longerons over time. In the experiment in air, the strip reaches its final height after 950 ms, never overshooting above the vertical location of the pulleys. In vacuum, the vertical motion was much faster and the maximum height was reached after 550 ms.

In summary, the experiments show that, for the suspension system concept studied in this paper (and for the chosen values of H_0 and M), the elastic folds do not propagate and essentially behave as fixed, self-latching elastic hinges, deploying in a consistent and repeatable fashion. If the structure is folded in a symmetric way, symmetry is also preserved throughout the deployment, which is very advantageous as it simplifies the development of mathematical models to predict the dynamics of the structure.

V. Numerical Model

A finite element model of the strip deployment was developed in Simulia Abaqus 2020 and is shown in Fig. 17. The TRAC longerons were modeled with S4R reduced-integration shell elements, and their material properties were defined using direct specification of the ABD matrix for the flanges and the web, based on previous measurements on coupons of a similar laminate [41]. The battens were modeled with B31 linear beam elements, with isotropic material model. The Ω-shaped connectors between longerons and battens were assumed to be rigid, and modeled as kinematic

coupling constraints between the end node of the battens and a region of the longeron web of the same size as the physical connector. The suspension system was modeled using a combination of 2D connector elements. More details about this model are provided later in this section. The membrane was bonded to the web of the longerons and to the battens using tie constraints. A uniform mesh of approximately 2 mm × 2 mm in size was used for all the parts of the model. Based on the essentially symmetric deployment observed in experiment, symmetry about the mid-plane of the strip was assumed for the finite element model, reducing the total number of elements by a factor 2. The resulting model contained 81,355 nodes and 79,556 elements, i.e. 24,156 shell elements and 54,900 membrane elements.

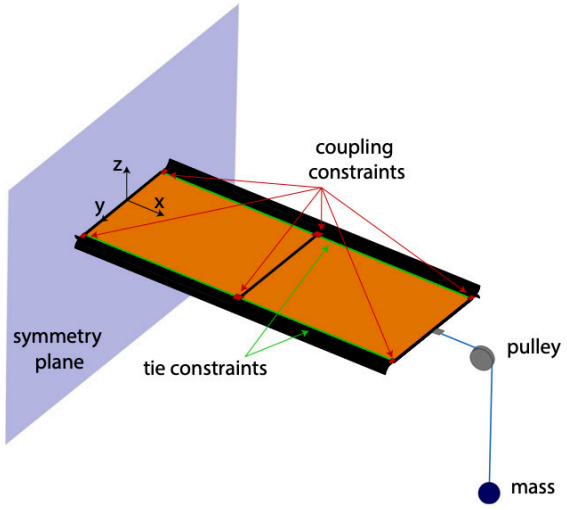

(a) Finite element model of a symmetric strip. Longerons and battens are connected by rigid coupling constraints; tie constraints connect the longerons to the membrane.

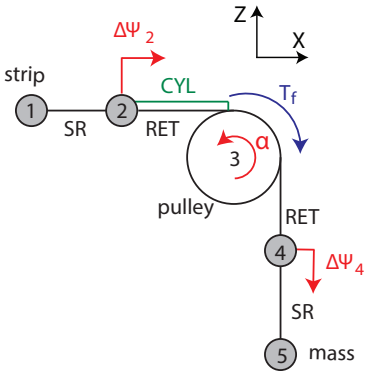

(b) Schematic of suspension system model, using 2D connector elements. Slip ring (SR) elements model the cord passing over the pulley; retractor (RET) elements convert the motion of the cords in rotation of the pulley. Cylindrical (CYL) elements introduce friction in the pulley.

Fig. 17 Description of the finite element model of a strip with membrane.

A. Membrane Formulation

Because of their small thickness, membranes have very small bending stiffness and cannot sustain any in-plane compressive loads. It is well known that wrinkling instabilities arise whenever the principal stress components in a membrane have opposite sign. A detailed numerical characterization of the wrinkles, in terms of wavelength and amplitude, requires a shell element formulation, capable of capturing the small, but still finite, bending stiffness of the membrane [44]. However, this approach is computationally expensive, as very fine meshes are required to accurately capture the short wavelength of the wrinkles. On the other hand, it has been shown [44] that the onset and orientation of the wrinkles can still be predicted accurately with less expensive membrane elements, by implementing a wrinkling theory into an *ad hoc* material model, known as the Iterative Material Model (IMP) [45][46]. This model is based on a mixed stress/strain criterion to identify three regimes for the membrane: slack, wrinkled and taut.

Each of these regions is associated with a different tangent stiffness matrix D under plane stress. When the membrane is taut, the constitutive relation is based on the standard relation for an isotropic membrane. A slack state corresponds to no stress in the membrane, hence the stiffness matrix D_s is null. Finally, when the membrane is wrinkled, an effective stiffness matrix D_w is defined, based on the assumption that the wrinkles are aligned with the principal stress in the

material, and that the stress is zero in the direction normal to the wrinkles. The resulting model is expressed as:

$$D_s = 0 \tag{5a}$$

$$D_w = \frac{E}{2}\begin{bmatrix} 2(1+P) & 0 & Q \\ 0 & 2(1-P) & Q \\ Q & Q & 1 \end{bmatrix} \tag{5b}$$

$$D_t = \frac{E}{1-\nu^2}\begin{bmatrix} 1 & \nu & 0 \\ \nu & 1 & 0 \\ 0 & 0 & (1+\nu)/2 \end{bmatrix} \tag{5c}$$

where E is the elastic modulus and the parameters P and Q are functions of the engineering strains ϵ_x, ϵ_y and γ_{xy}, defined as:

$$P = \frac{\epsilon_x - \epsilon_y}{\epsilon_1 - \epsilon_2} \tag{6a}$$

$$Q = \frac{\gamma_{xy}}{\epsilon_1 - \epsilon_2} \tag{6b}$$

where ϵ_1 and ϵ_2 are the principal strains.

Various implementations of the IMP algorithm have been successfully used in finite element codes, both with implicit [47] and explicit [48] integration schemes. Hence, an implementation of the IMP model as a VUMAT was used in the Abaqus Explicit simulations presented in the rest of this paper.

B. Suspension System Model

The suspension system was modeled using connector elements. In the literature, the problem of modeling cables and pulleys has been discussed in the context of cranes, electrical transmission lines and seat belts. Aufaure [49] developed a model to capture sagging of electrical transmission lines under self-weight. The cables were modeled as truss elements, on which a zero-dimensional frictionless pulley was allowed to slide. Ju et al. [50] proposed a formulation that accounted for friction between cord and pulley, which results in having different tension in the cord segments on the two sides of the pulley. A super-element formulation was also proposed to include multiple pulleys in crane systems. However, inertial effects in the pulley were not considered.

In dynamic simulations of automotive crash events [51] [52], the seat belt systems are often modeled using combinations of slip ring and retractor elements. Slip rings are 2-node elements that enable a "material flow" degree of freedom at their nodes. This allows mass to enter or exit the element, which therefore increases or reduces its length without elastic deformations. Connecting two slip rings in series, the mass exiting from one element enters the other element though their shared node, effectively modeling the passage of two portions of a belt over a D-ring or buckle in a seat belt system. Retractor elements, instead, convert the material flow at one node into rotation of the other node, and they are used to model the belt spooling from the retractor mechanism. These elements are built-in in commercial finite element software, like LS Dyna and Abaqus, hence they were chosen for the strip deployment simulations developed in this paper.

A schematic of the FE model is shown in Fig. 17(b): the circles 1-5 represent nodes of the connector elements. Node 1 corresponds to the strip-cord connector and it is connected to the central nodes of the strip outermost batten using MPC beam constraints. Node 3 is the pulley, which has only one rotational degree of freedom about the y-axis. Node 5 represents the counterweight attached to the end of the cord, whereas nodes 2 and 4 are auxiliary intermediate nodes. Slip ring elements model the cords, connecting nodes 1-2 and 4-5. To prevent the cords from experiencing axial compression during dynamic loading, a bi-linear elastic model is assigned to the slip rings, with tensile stiffness $K_t = 1000$ N/mm and compressive stiffness $K_c = 1$ N/mm. A sensitivity study for these parameters showed that, under the expected loads in simulation, the cords effectively behave as rigid in tension and slack in compression.

To take into account the inertial effects in the pulley, retractor elements between 2-3 and 4-3 convert the material flow at nodes 2 and 4 into rotation of node 3, according to the equation:

$$\alpha = \frac{\Delta\Psi_2}{R} = \frac{\Delta\Psi_4}{R} \tag{7}$$

with R being the radius of the pulley and $\Delta\Psi_2$ and $\Delta\Psi_4$ the material flow at nodes 2 and 4 (note that, since the retractor elements are connected in series, the material flow is the same on both nodes).

Lastly, friction in the pulley bearing was captured by adding a second connector element between nodes 2 and 3, in parallel with the retractor element. This element models a cylindrical joint, constraining all relative displacements between its nodes, except for the relative rotation about the y-axis. It provides the friction torque associated with the rotational degree of freedom, through the relationship:

$$T_3 = -\text{sign}(\alpha)T_f \tag{8}$$

where T_f is constant and is obtained from the experimental characterization of the suspension system described in Sec. III.D. The experiment described in Sec. III.D was used as a benchmark to verify the numerical model of the suspension system, whose results showed very good agreement both with the analytical solution and the experiment.

C. Air Model

The effect of air on the dynamics of lightweight large-area structures has been investigated in literature in the contexts of vibration of membranes. It has been shown that membranes vibrating in air have lower natural frequencies and higher damping than in vacuum [53].

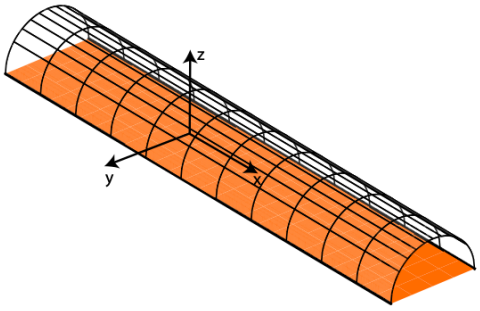

Fig. 18 Volume of air mass added to the strip model with membrane.

Analytical solutions for simple geometries [54] have proven that the effect of air pressure in the equations of motion can be described in terms of a frequency-dependent added mass. A variety of numerical approaches have been proposed to estimate the added air mass, using different levels of fidelity. Sewell [55] used a geometric argument to define an effective air volume for triangular membranes. The resulting air mass, assumed constant, was distributed in a non-uniform fashion, in order to be maximum at the center of the membrane and zero at the edges. Higher fidelity models have been developed to explicitly include the air around the membrane, either using the boundary element method [56] or defining an air box with finite elements [54]. To the authors' knowledge, there has not been any previous attempt at predicting the effect of air on large-displacement deployment problems.

Therefore, to avoid the significant computational cost associated with high fidelity models of such interaction, in this paper a simple model inspired by [55] was adopted. Specifically, it was assumed that the main contribution to the added mass comes from the air volume further away from the edges of the structure, which is forced to move with the structure. Due to the high aspect ratio of the strip, a half-cylindrical volume around the strip was therefore considered, as shown in Fig. 18.

The height of air in the volume above the structure only varies with its transverse coordinate, and is described by:

$$z_a(y) = \sqrt{\left(\frac{W}{2}\right)^2 - y^2} \tag{9}$$

where W is the width of the strip. The corresponding mass of air is:

$$m_a = \rho_a L \int_{-\frac{W}{2}}^{\frac{W}{2}} z(y)dy = \frac{\pi \rho_a W^2 L}{8} \tag{10}$$

with $\rho_a = 1.225\ kg/m^3$ being the standard air density.

The added air mass was uniformly distributed over the area of the Kapton membrane by scaling its mass with the factor:

$$K = \frac{m_k + m_a}{m_k} \tag{11}$$

where m_k is the mass of the membrane. From an implementation standpoint, the added air mass could be introduced by increasing the density of the membrane. However, this would increase not only the inertia of the structure during deployment, but also its gravity loading, thus altering the starting folded configuration, as well as the height of the structure in its fully deployed state. Therefore, the added air mass was introduced using mass scaling, which is a technique often used in quasi-static problems with explicit solvers. Mass scaling has the advantage of increasing the density of the material and, therefore, the stable time increment of the solver, drastically reducing the number of increments needed to perform long simulations. The mass scaling formulation in Abaqus only affects the inertial term in the equations of motion of the model, but it is not included in the calculation of gravity loads. Therefore, it is ideal to model the effect of air on the dynamics of the structure, without affecting its equilibrium configuration.

Based on this model, the added air mass for a strip with membrane deploying in air is $m_a = 31.7$ g. The added mass due to the residual air in the experiments in vacuum is 3.0 g, and it was neglected in simulation. For the strip without membrane, the air volume to consider would consist of two half-cylinders, with diameter equal to the width of the longerons. The resulting added mass for the deployment in air and vacuum would be 0.45 g and 0.04 g, respectively. They were both neglected for the purpose of this analysis.

Therefore, air was only included in the simulation of the strip with membrane deploying in air; the resulting mass scaling was $K = 3.0$.

D. Simulation Strategy

The simulations were performed in Abaqus explicit and were organized as follows:

1) In the first step, gravity was applied to tension the cord. Localized folds were induced on the longerons by pressure loads distributed on both flanges, over a 20 mm long region; the size of this region was chosen so as to include enough elements to avoid locking of the mesh induced by excessive shearing.
2) A rigid cylinder with radius equal to the flange radius was used to push the strip into its folded configuration, using displacement control.
3) In the equilibrium step, the residual kinetic energy was dissipated until it was decreased to less than 1% of the maximum strain energy.
4) Finally, in the deployment step, the cylinders were instantaneously removed and the structure was allowed to self-deploy.

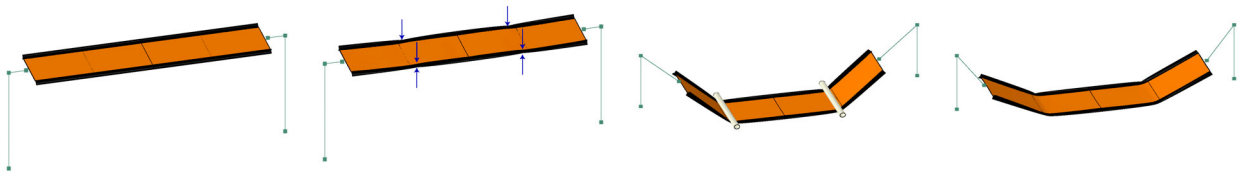

(a) Initial configuration (b) Create localized folds (c) Folding (d) Deployment

Fig. 19 Simulation sequence: first, gravity is applied and the longerons are pinched to create localized folds (b). Then, rigid cylinders are used to fold the structure (c). An equilibrium step helps to dissipate any residual kinetic energy to reach the initial condition.

In the initial part of the simulation, numerical damping was used to reduce dynamic effects on the structure. Previous studies have shown that a velocity-dependent viscous pressure, defined as $p = -c_v \mathbf{v} \cdot \mathbf{n}$, is very effective at dissipating high order vibrations in deployment problems of thin shell structures [28][57].

However, sensitivity studies on the strip deployment suggested that small amounts of linear damping, proportional to the volumetric strain of the element, are also beneficial to prevent numerical instabilities. Hence, a combination of both damping models was used. Table 2 summarizes the main parameters for each of the simulation steps described above.

Step	Duration [s]	Linear damping λ	Viscous pressure c_v
1. Gravity	0.1	10^{-4}	10^{-8}
2. Folding	0.5	10^{-4}	10^{-8}
3. Equilibrium	0.3	10^{-4}	10^{-7}
4. Deployment	1.0	10^{-8}	0

Table 2 Simulation parameters

In the first three steps, the step time was chosen so as to achieve the correct folded configuration before deployment, in the shortest computational time possible. With these settings, a simulation using 8 CPUs on a server with 3.5 GHz Intel Xeon Gold 6144 processor took about 83 hours 45 minutes (30 hours 20 minutes for folding, 53 hours 25 minutes for deployment) for a strip with membrane, 25 hours 25 minutes for a strip without membrane (17 hours 20 minutes for folding, 8 hours 5 minutes for deployment).

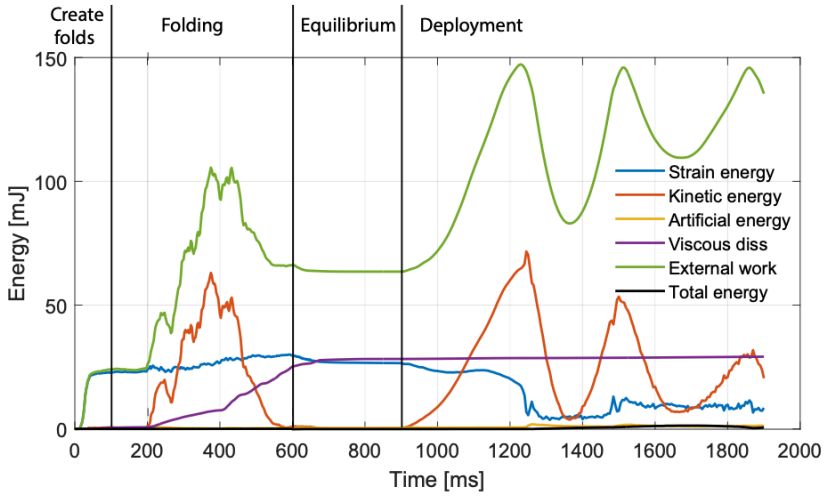

Fig. 20 Energy balance for strip with membrane deploying in air. Initial conditions: $H_0 = 400$ **mm,** $\lambda_0 = 0.45$**,** $M = 50$ **g.**

Figure 20 shows the energy balance for the simulation of a strip with membrane, deploying in air. The total energy (in black) remains constant and equal to zero throughout the simulation, confirming that there is no energy loss from the model. The artificial energy, associated with hourglassing modes in the finite element mesh, is very small throughout the simulation. The viscous dissipation increases during the folding process and is associated with the viscous pressure introduced during that step. In the deployment phase, the viscous dissipation remains approximately constant, confirming that the dynamics of the structure are not altered by numerical viscous effects. Regarding the strain energy of the strip, the largest contribution comes from the formation of elastic folds by pinching the longerons, in the first step of the simulation. During folding, additional strain energy is stored due to the increase in the angle of the folds. After deployment, most of the strain energy is released, but it does not fully return to zero, due to residual elastic deformations associated with vibrations of the deployment strip.

The energy balance also indicates that the folding process is not quasi-static, since the kinetic energy is very high compared to the strain energy in the strip. However, the kinetic energy is almost entirely dissipated before the initiation of deployment, where it becomes less than 1% of the strain energy.

VI. Comparison between Numerical Results and Experiments

This section presents the results from the finite element model. First, the quasi-static unfolding of a strip is used as benchmark problem to validate the finite element model of the strip, comparing its results with the experimental data presented in Sec. III.B. Then, the deployment results are presented and compared with the experiments.

A. Model Validation

A quasi-static unfolding simulation of the strips was performed using an implicit solver in Abaqus. The boundary conditions matched the geometry and kinematics of the experimental setup described in Sec. III.B. The simulation was structured in 4 steps: first, a small pressure load was applied to the flanges at the center of the longerons, in order to facilitate the formation of elastic folds; then the strip was folded to an angle $\theta = 35°$; subsequently, the pressure load was removed without varying the applied rotation; finally, the strip was unfolded. The unfolding simulation showed that the strip undergoes several instabilities during the process, corresponding to propagation of the elastic folds. Such instabilities make convergence difficult to achieve; hence, a small amount of viscous stabilization was introduced to help the solver achieve equilibrium. A sensitivity analysis of this parameter showed that a maximum allowable ratio of stabilization energy to total strain energy on the order of 10^{-7} provides sufficient stabilization with negligible effect on the predicted moment in the strip. However, larger stabilization was required in the final part of unfolding, where snapping of the elastic folds releases significant amounts of energy.

The results are shown in Fig. 21 for the strip with and without membrane. Overall, the simulations are in good agreement with the experiments for large angles ($\theta > 10°$) correctly capturing the steady-state moment of the strip. For smaller angles, where the localized fold disappear, simulations significantly overpredict the peak moment, which is 3 times higher than the measurement for the strip without membrane, 1.4 times higher for the strip with membrane.

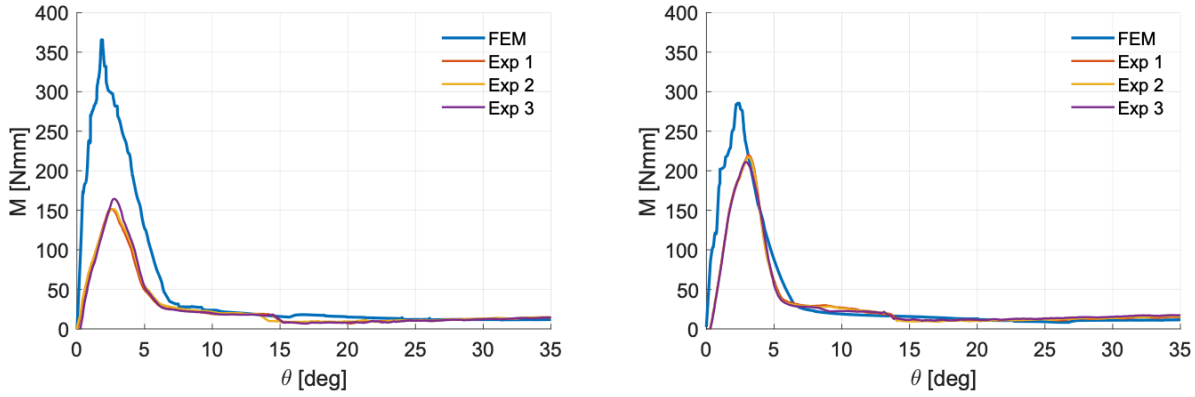

(a) Strip without membrane

(b) Strip with membrane

Fig. 21 Comparison between simulations and experiments for quasi-static unfolding of a strip.

Two reasons can be identified for this discrepancy. First, as explained in Sec. III.B, experiments show that localized folds transition from a symmetric to an asymmetric configuration when $\theta \approx 15°$, then they turn into a local flange buckling at the peak moment, before gradually disappearing as the applied rotation is reduced. Simulations miss the transition to the asymmetric fold, hence following a higher energy equilibrium path, which results in higher peak moment.

This difference in behavior is not surprising, as it is well known that thin shell structures exhibit multiple energetically-similar equilibrium paths, the choice of which is very sensitive to small geometric imperfections in the structure. Therefore, since no imperfections were introduced in the simulation, the model follows the most symmetric equilibrium solution, which is not necessarily the lowest energy path. For the same reason, the localized folds on the two longerons disappear at the same time in simulation. In experiment, this only happens for the strip with membrane, which explains why the error is smaller in this case. This suggests that the coupling between the longerons introduced by the membrane might help making the structure less sensitive to imperfections, leading to a more deterministic and predictable behavior.

B. Comparison of Deployment Results

This section compares the results of the deployment simulations to the experiments done on both strips (with and without membrane), both in air and in vacuum. The plots shown present the evolution of the fold angle and height of the center of the strip as a function of time. Blue and orange lines represent experiments and simulations, respectively. Different runs of the same experiment are indicated by solid, dashed and dotted lines.

Figure 22 shows the results for a strip without membrane. The simulation closely matches the experiments both qualitatively and quantitatively. The fold angle decreases symmetrically on both longerons (hence only one of them is plotted) and oscillates during the process. The amplitude and period of the oscillations are well captured by the simulation, and the deployment time is 4 % slower than the mean deployment time from experiments. When the fold angles become zero for the first time, latching of the elastic folds occurs and the strip undergoes elastic vibrations. The plot on the right hand side shows the evolution of the height of the center of the strip. Simulation and experiments start from the same height (400 mm below the position of the pulleys), and they match very closely for the initial 250 ms of deployment. After that, the simulation becomes slightly faster than the experiment and reaches a 30 mm higher peak height.

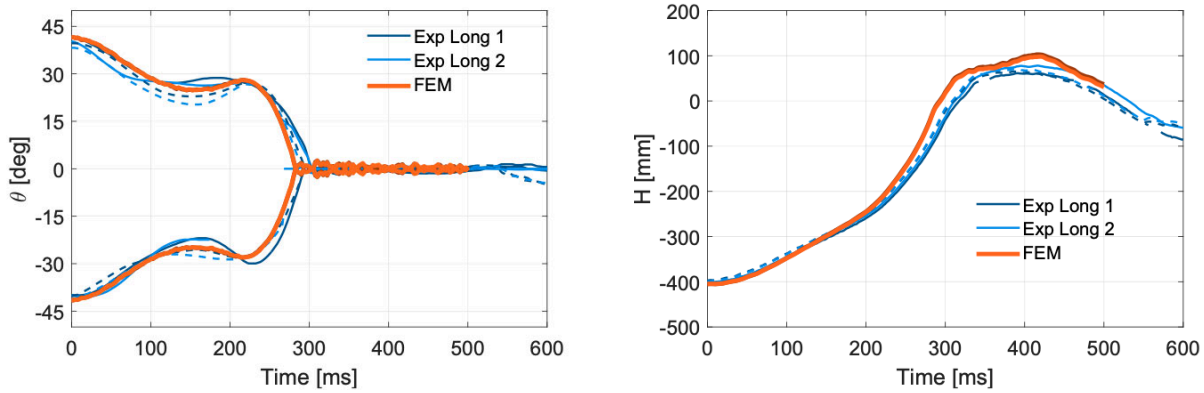

(a) Fold angles

(b) Center height

Fig. 22 Comparison between experiments in vacuum and simulations for a strip without membrane. Initial conditions: $H_0 = 400$ **mm,** $\lambda_0 = 0.45$**,** $M = 50$ **g.**

Figures 23(a) and 23(b) show the results for a strip with membrane, deploying in vacuum. Again, there is very good agreement between simulation and experiments, with the predicted fold angle being within the envelope of experimentally measured angles, and the predicted deployment time being less than 5 % slower than the mean experimental value. Regarding the height of the center of the strip, the simulation starts from the same value as the experiment, but becomes slightly slower after 150 ms, maintaining a 30 mm constant offset after this point. However, at the end of deployment, it reaches the same maximum height at approximately the same time.

Figures 23(c) and 23(d) present the results for a strip with membrane deploying in air. The deployment time is correctly captured by the simulation, although the fold angle oscillates more than observed in the experiment. Good agreement is also found in the height of the structure, although the finite element model is slower than the experiment in the first 400 ms of deployment, and it becomes faster afterwards.

VII. Discussion and Conclusion

This paper has presented a detailed study of the dynamic deployment of a flexible rectangular strip, composed of interconnected thin shell components. The strip was initially folded with two elastic folds, and deployed by its stored elastic energy. An experimental setup was designed to symmetrically fold 1 m-scale structural prototypes, which were supported by a cord suspension system and deployed against gravity. Digital Image Correlation was used to measure the deformation of the structure during deployment, and to track the location and angle of the elastic folds.

Experiments showed that the structure remains essentially symmetric during the process, and that elastic folds do not propagate, but rather behave as non-linear elastic hinges. It is interesting to notice that this behavior is quite different from that of a folded tape spring, whose elastic fold has been shown to propagate significantly during dynamic unfolding

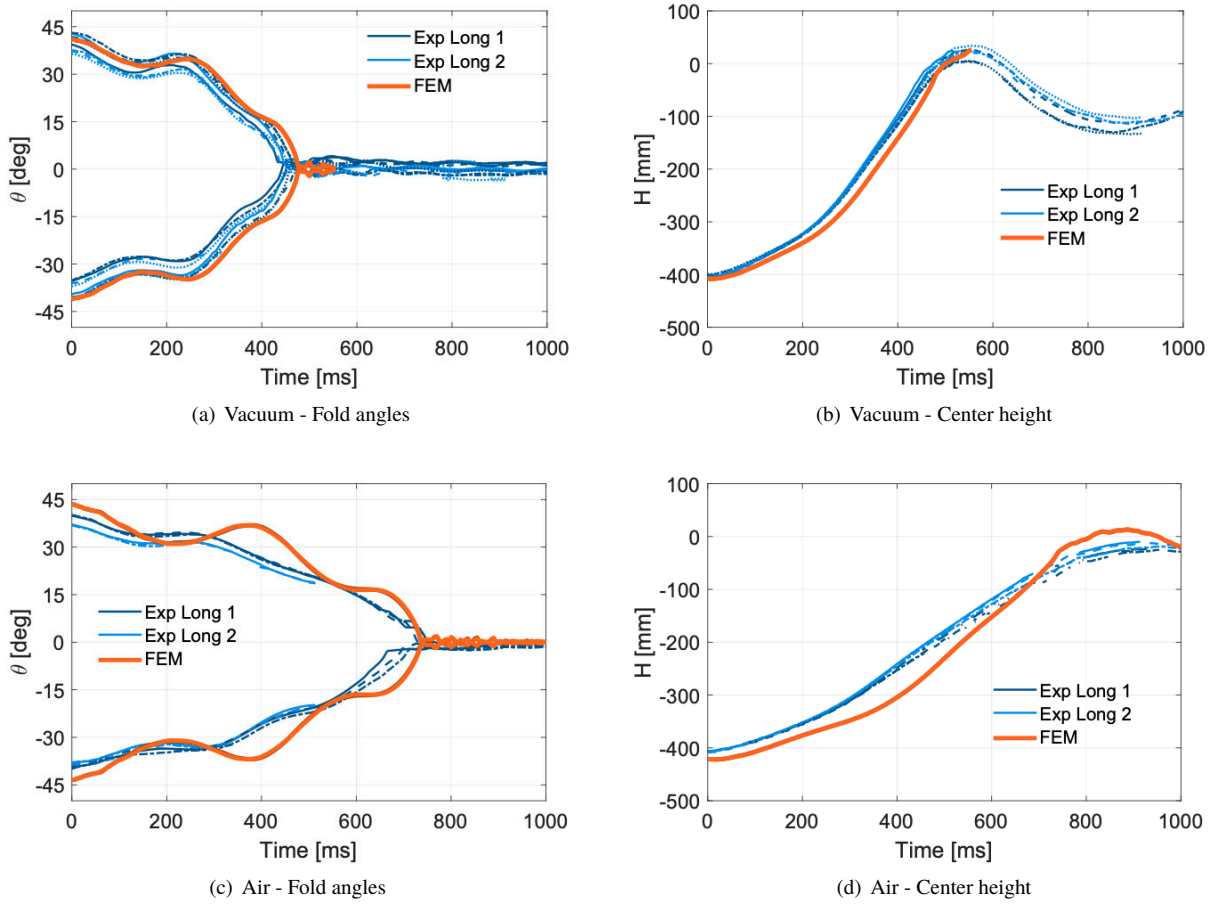

(a) Vacuum - Fold angles

(b) Vacuum - Center height

(c) Air - Fold angles

(d) Air - Center height

Fig. 23 Comparison between experiments and simulations for a strip with membrane. Initial conditions: $H_0 = 400$ **mm,** $\lambda_0 = 0.45$**,** $M = 50$ **g.**

[23]. It is not clear yet whether this difference is intrinsic in the strip architecture and results from the interaction between its thin shell components, or if it is an artifact of external factors, such as gravity and boundary conditions. In future, deployment experiments in different orientations or simulations of deployment in micro-gravity might provide additional insight into this question.

The effect of air on the deployment dynamics of these structures has been experimentally characterized for the first time. It has been shown that the interaction with air significantly slows down the deployment of a strip prototype supporting a thin membrane. However, this effect becomes negligible in the absence of the membrane.

A finite element model of deployment has been developed. The simulations can accurately capture the initial equilibrium configuration in the folded state, and predict the deployment time measured in the experiments with less than 5 % error.

A simple model to predict the added mass of air based on the geometry of the structure has been proposed. Simulations made with this model closely match the deployment time measured in the experiments. Although the global deployment behavior is correctly captured, the finite element model tends to overpredict the amplitude and period of the oscillations of the fold angle occurring during deployment. This suggests that including air added mass in the simulation may not be sufficient to fully describe its interaction with the structure, and an air drag model might also be needed.

On the experimental side, it may be interesting to consider alternative suspension system designs, to examine the effects of reducing the influence of gravity, for example by arranging for the structure to deploy horizontally. Also, while the present study has considered initial folding angles of about 45°, it would be interesting to investigate the deployment of fully folded strips.

While more work is required both on experimental and computational aspects of this problem, the results in this

paper suggest that, at least under the examined conditions, shell-based space frames can self-deploy in a reliable and repeatable fashion. This represents a promising path forward to the application of thin shell technologies to novel lightweight solar array concepts and other applications.

Acknowledgements

The authors thank Dr. Xiaowei Deng (University of Hong Kong) for providing the Abaqus subroutine implementing the IMP membrane formulation, Alan Truong (Caltech) for building the strip prototypes used in the experiments in this paper, Charles Sommer (Caltech) for assisting with the deployment experiments in vacuum, and Fabien Royer (Caltech) for help with the bending tests of the strip prototypes. Financial support from the Space Solar Power Project at Caltech is gratefully acknowledged.

References

[1] Surampudi, R., Hamilton, T., Rapp, D., Stella, P., Mardesich, N., Mondt, J., Nesmith, B., Bunker, R. L., Cutts, J., Bailey, S. G., Curtis, H. B., Piszczor, M., Gaddy, E., Marvin, D., and Kazmerzki, L., "Solar cell and array technology for future space missions," Tech. rep., Technical Report D-24454, National Aeronautics and Space Administration, 2002.

[2] Jones, P. A., and Spence, B. R., "Spacecraft solar array technology trends," *IEEE Aerospace and Electronic Systems Magazine*, Vol. 26, No. 8, 2011, pp. 17–28.

[3] Kwak, M. K., Heo, S., and Kim, H. B., "Dynamics of satellite with deployable rigid solar arrays," *Multibody System Dynamics*, Vol. 20, No. 3, 2008, pp. 271–286.

[4] Jeong, J. W., Yoo, Y. I., Lee, J. J., Lim, J. H., and Kim, K. W., "Development of a tape spring hinge with a SMA latch for a satellite solar array deployment using the independence axiom," *Ieri Procedia*, Vol. 1, 2012, pp. 225–231.

[5] Sauder, J. F., Arya, M., Chahat, N., Thiel, E., Dunphy, S., Shi, M., Agnes, G., and Cwik, T., "Deployment mechanisms for high packing efficiency one-meter reflectarray antenna (OMERA)," *AIAA Scitech 2019 Forum*, 2019-0755.

[6] Wu, S.-C., and Ghofranian, S., "Anomaly simulation and resolution of International Space Station solar array deployment," *Modeling, Simulation, and Verification of Space-based Systems II*, Vol. 5799, International Society for Optics and Photonics, 2005, pp. 38–47.

[7] Klesh, A., and Krajewski, J., "MarCO: CubeSats to Mars in 2016," *Proceedings of the 29th Annual AIAA/USU Conference on Small Satellites*, 2015.

[8] Hausgen, P. E., Carpenter, B., Gupta, N., and Turse, D., "TacSat 2 experimental solar array on-orbit data and analysis," *2016 IEEE 43rd Photovoltaic Specialists Conference (PVSC)*, IEEE, 2016, pp. 2565–2570.

[9] Olson, G., Murphey, T., and Thomas, G., "Free deployment dynamics of a Z-folded solar array," *52nd AIAA/ASME/ASCE/AHS/ASC Structures, Structural Dynamics and Materials Conference 19th AIAA/ASME/AHS Adaptive Structures Conference 13t*, 2011-1730.

[10] Mikulas, M. M., Pappa, R. S., Warren, J., and Rose, G., "Telescoping solar array concept for achieving high packaging efficiency," *2nd AIAA Spacecraft Structures Conference*, 2015-1398.

[11] Jorgensen, J., Louis, E., Hinkle, J., Silver, M., Zuckermandel, B., and Enger, S., "Dynamics of an elastically deployable solar array: ground test model validation," *46th AIAA/ASME/ASCE/AHS/ASC Structures, Structural Dynamics and Materials Conference*, 2005-1942.

[12] Yang, D., Yang, R., Priya, S., and Liu, S., "Recent advances in flexible perovskite solar cells: fabrication and applications," *Angewandte Chemie International Edition*, Vol. 58, No. 14, 2019, pp. 4466–4483.

[13] Hashemi, M. R. M., Fikes, A. C., Gal-Katziri, M., Abiri, B., Bohn, F., Safaripour, A., Kelzenberg, M. D., Warmann, E. L., Espinet, P., Vaidya, N., Gdoutos, E. E., Leclerc, C., Royer, F., Pellegrino, S., Atwater, H. A., and Hajimiri, A., "A flexible phased array system with low areal mass density," *Nature Electronics*, Vol. 2, No. 5, 2019, pp. 195–205.

[14] Jordan, R., Picardi, G., Plaut, J., Wheeler, K., Kirchner, D., Safaeinili, A., Johnson, W., Seu, R., Calabrese, D., Zampolini, E., Cicchetti, R., Huff, R., Gurnett, D., Ivanov, A., Kofman, W., Orosei, R., Thompson, T., Edenhofer, P., and Bombaci, O., "The Mars express MARSIS sounder instrument," *Planetary and Space Science*, Vol. 57, No. 14-15, 2009, pp. 1975–1986.

[15] Biddy, C., and Svitek, T., "LightSail-1 solar sail design and qualification," *Proceedings of the 41st Aerospace Mechanisms Symposium*, Jet Propulsion Lab., National Aeronautics and Space Administration Pasadena, CA, 2012, pp. 451–463.

[16] Spence, B. R., White, S., LaPointe, M., Kiefer, S., LaCorte, P., Banik, J., Chapman, D., and Merrill, J., "International space station (ISS) roll-out solar array (ROSA) spaceflight experiment mission and results," *2018 IEEE 7th World Conference on Photovoltaic Energy Conversion (WCPEC)(A Joint Conference of 45th IEEE PVSC, 28th PVSEC & 34th EU PVSEC)*, IEEE, 2018, pp. 3522–3529.

[17] Seefeldt, P., Spietz, P., Sproewitz, T., Grundmann, J. T., Hillebrandt, M., Hobbie, C., Ruffer, M., Straubel, M., Tóth, N., and Zander, M., "Gossamer-1: Mission concept and technology for a controlled deployment of gossamer spacecraft," *Advances in Space Research*, Vol. 59, No. 1, 2017, pp. 434–456.

[18] Fernandez, J. M., Rose, G. K., Younger, C. J., Dean, G. D., Warren, J. E., Stohlman, O. R., and Wilkie, W. K., "NASA's Advanced Solar Sail Propulsion System for Low-Cost Deep Space Exploration and Science Missions that Use High Performance Rollable Composite Booms," *4th International Symposium on Solar Sailing*, 2017.

[19] Heidt, H., Puig-Suari, J., Moore, A., Nakasuka, S., and Twiggs, R., "CubeSat: A new generation of picosatellite for education and industry low-cost space experimentation," *14th Annual/USU Conference on Small Satellites*, 2000.

[20] Thurn, A., Huynh, S., Koss, S., Oppenheimer, P., Butcher, S., Schlater, J., and Hagan, P., "A nichrome burn wire release mechanism for CubeSats," *The 41st Aerospace Mechanisms Symposium, Jet Propulsion Laboratory*, 2012, pp. 479–488.

[21] Guzik, A. T., and Benafan, O., "Design and Development of CubeSat Solar Array Deployment Mechanisms Using Shape Memory Alloys," *44th Aerospace Mechanisms Symposium*, 2018.

[22] Arya, M., Lee, N., and Pellegrino, S., "Ultralight structures for space solar power satellites," *3rd AIAA Spacecraft Structures Conference*, 2016-1950.

[23] Seffen, K., and Pellegrino, S., "Deployment dynamics of tape springs," *Proceedings of the Royal Society of London. Series A: Mathematical, Physical and Engineering Sciences*, Vol. 455, No. 1983, 1999, pp. 1003–1048.

[24] Calladine, C., "The theory of thin shell structures 1888–1988," *Proceedings of the Institution of Mechanical Engineers, Part A: Power and Process Engineering*, Vol. 202, No. 3, 1988, pp. 141–149.

[25] Wuest, W., "Einige anwendungen der theorie der zylinderschale," *ZAMM-Journal of Applied Mathematics and Mechanics/Zeitschrift für Angewandte Mathematik und Mechanik*, Vol. 34, No. 12, 1954, pp. 444–454.

[26] Rimrott, F., "Nachtrag zum Tagungsheft der GAMM-Tagung 1969. Querschnittsverformung bei Torsion offener Profile," *ZAMM-Journal of Applied Mathematics and Mechanics/Zeitschrift für Angewandte Mathematik und Mechanik*, Vol. 50, No. 12, 1970, pp. 775–778.

[27] Mansfield, E. H., "Large-deflexion torsion and flexure of initially curved strips," *Proceedings of the Royal Society of London. A. Mathematical and Physical Sciences*, Vol. 334, No. 1598, 1973, pp. 279–298.

[28] Mallikarachchi, H., and Pellegrino, S., "Deployment dynamics of ultrathin composite booms with tape-spring hinges," *Journal of Spacecraft and Rockets*, Vol. 51, No. 2, 2014, pp. 604–613.

[29] Marks, G. W., Reilly, M. T., and Huff, R. L., "The lightweight deployable antenna for the MARSIS experiment on the Mars express spacecraft," *36th Aerospace Mechanisms Symp*, 2002, pp. 183–196.

[30] Royer, F., and Pellegrino, S., "Ultralight ladder-type coilable space structures," *2018 AIAA Spacecraft Structures Conference*, 2018-1200.

[31] Roybal, F., Banik, J., and Murphey, T., "Development of an elastically deployable boom for tensioned planar structures," *48th AIAA/ASME/ASCE/AHS/ASC Structures, Structural Dynamics, and Materials Conference*, 2007-1838.

[32] Lekan, J., "Microgravity research in NASA ground-based facilities," *27th Aerospace Sciences Meeting*, 1989-236.

[33] Steinberg, T., "Reduced gravity testing and research capabilities at Queensland University of Technology's New 2.0 Second Drop Tower," *Advanced Materials Research*, Vol. 32, Trans Tech Publ, 2008, pp. 21–24.

[34] Block, J., Bäger, A., Behrens, J., Delovski, T., Hauer, L.-C., Schütze, M., Schütze, R., and Spröwitz, T., "A self-deploying and self-stabilizing helical antenna for small satellites," *Acta Astronautica*, Vol. 86, 2013, pp. 88–94.

[35] Firth, J., Adamcik, B., Hannah, E., Firth, D., and Pankow, M., "Minimal Unpowered Strain-Energy Deployment Mechanism for Rollable Spacecraft Booms," *AIAA Scitech 2019 Forum*, 2019-1258.

[36] Mao, H., Ganga, P. L., Ghiozzi, M., Ivchenko, N., and Tibert, G., "Deployment of bistable self-deployable tape spring booms using a gravity offloading system," *Journal of Aerospace Engineering*, Vol. 30, No. 4, 2017-04017007.

[37] Greschik, G., and Belvin, W. K., "High-fidelity gravity offloading system for free-free vibration testing," *Journal of Spacecraft and Rockets*, Vol. 44, No. 1, 2007, pp. 132–142.

[38] Fischer, A., and Pellegrino, S., "Interaction between gravity compensation suspension system and deployable structure," *Journal of Spacecraft and Rockets*, Vol. 37, No. 1, 2000, pp. 93–99.

[39] Han, O., Kienholz, D., Janzen, P., and Kidney, S., "Gravity-Offloading System for Large-Displacement Ground Testing of Spacecraft Mechanisms," *Proceedings of the 40th Aerospace Mechanisms Symposium*, 2010.

[40] Leclerc, C., Pedivellano, A., and Pellegrino, S., "Stress concentration and material failure during coiling of ultra-thin TRAC booms," *2018 AIAA Spacecraft Structures Conference*, 2018-0690.

[41] Leclerc, C., and Pellegrino, S., "Nonlinear elastic buckling of ultra-thin coilable booms," *International Journal of Solids and Structures*, Vol. 203, 2020, pp. 46–56.

[42] Royer, F., Li, Y., Truong, A., Sommer, C., and Pellegrino, S., "Pure Bending Machine for the Testing of Imperfection Sensitive Non-Linear Structures," In preparation.

[43] Houpert, L., "Ball bearing and tapered roller bearing torque: analytical, numerical and experimental results," *Tribology Transactions*, Vol. 45, No. 3, 2002, pp. 345–353.

[44] Wong, W., and Pellegrino, S., "Wrinkled membranes III: numerical simulations," *Journal of Mechanics of Materials and Structures*, Vol. 1, No. 1, 2006, pp. 63–95.

[45] Miller, R. K., and Hedgepeth, J. M., "An algorithm for finite element analysis of partly wrinkled membranes," *AIAA Journal*, Vol. 20, No. 12, 1982, pp. 1761–1763.

[46] Miller, R. K., Hedgepeth, J. M., Weingarten, V. I., Das, P., and Kahyai, S., "Finite element analysis of partly wrinkled membranes," *Advances and Trends in Structures and Dynamics*, Elsevier, 1985, pp. 631–639.

[47] Adler, A., and Mikulas, M., "Application of a wrinkled membrane finite element approach to advanced membrane structures," *AIAA Space 2001 Conference and Exposition*, 2001-4646.

[48] Deng, X., and Pellegrino, S., "Wrinkling of orthotropic viscoelastic membranes," *AIAA journal*, Vol. 50, No. 3, 2012, pp. 668–681.

[49] Aufaure, M., "A finite element of cable passing through a pulley," *Computers & Structures*, Vol. 46, No. 5, 1993, pp. 807–812.

[50] Ju, F., and Choo, Y. S., "Dynamic analysis of tower cranes," *Journal of engineering mechanics*, Vol. 131, No. 1, 2005, pp. 88–96.

[51] Fraterman, E., and Lupker, H., "Evaluation of belt modelling techniques," Tech. rep., SAE Technical Paper, 1993.

[52] Hughes, K., Gulavani, O., Vuyst, T. D., and Vignjevic, R., "Explicit dynamic formulation to demonstrate compliance against quasi-static aircraft seat certification loads (CS25. 561)–Part II: Influence of body blocks," *Proceedings of the Institution of Mechanical Engineers, Part G: Journal of Aerospace Engineering*, Vol. 228, No. 10, 2014, pp. 1890–1903.

[53] Yasaka, T., and Oda, S., "Air effects on the structure vibration and the considerations to large spacecraft ground testing," *39th Congress of the International Astronautical Federation*, 1988.

[54] Kukathasan, S., and Pellegrino, S., "Vibration of prestressed membrane structures," *University of Cambridge*, 2000.

[55] Sewell, J., Miserentino, R., and Pappa, R. S., "Vibration studies of a lightweight three-sided membrane suitable for space application," *NASA Technical Paper*, 1983.

[56] Sygulski, R., "Dynamic analysis of open membrane structures interacting with air," *International journal for numerical methods in engineering*, Vol. 37, No. 11, 1994, pp. 1807–1823.

[57] Sakovsky, M., and Pellegrino, S., "Closed cross-section dual-matrix composite hinge for deployable structures," *Composite Structures*, Vol. 208, 2019, pp. 784–795.